A *CloudSat* Perspective on the Cloud Climatology and Its Association with Aerosol Perturbations in the Vertical over Eastern China

TIANMENG CHEN,[a] JIANPING GUO,[b] ZHANQING LI,[a,c] CHUANFENG ZHAO,[a]
HUAN LIU,[b] MAUREEN CRIBB,[c] FU WANG,[d] AND JING HE[b]

[a] *State Key Laboratory of Earth Surface Processes and Resource Ecology, and College of Global Change
and Earth System Science, Beijing Normal University, Beijing, China*
[b] *State Key Laboratory of Severe Weather, Chinese Academy of Meteorological Sciences, Beijing, China*
[c] *Department of Atmospheric and Oceanic Science, and Earth System Science Interdisciplinary Center,
University of Maryland, College Park, College Park, Maryland*
[d] *National Satellite Meteorological Center, China Meteorological Administration, Beijing, China*

ABSTRACT

Many efforts have been taken to investigate aerosol–cloud interactions from space, but only a few studies have examined the response of vertical cloud structure to aerosol perturbations. Three-dimensional cloud climatologies of eight different cloud types identified from the *CloudSat* level-2 cloud product during the warm season (May–September) in 2008–10 over eastern China were first generated and analyzed. Using visibility as a proxy for cloud condensation nuclei, in combination with satellite-observed radar reflectivity, normalized contoured frequency by altitude diagrams of the differences in cloud radar reflectivity Z profiles under polluted and clean conditions were constructed. For shallow cumulus clouds (shallow Cu) Z tends to be inhibited, and it is enhanced in the upper layers for deep cumulus (deep Cu), nimbostratus (Ns), and deep convective clouds (DCC) under polluted conditions. Overall, analyses of the modified center of gravity (MCOG) and cloud-top height (CTH) also point to a similar aerosol effect, except for the nonsignificant changes in MCOGs and CTHs in deep Cu. The impacts of environmental factors such as lower-tropospheric stability and vertical velocity are also discussed for these types of clouds. Although consistent aerosol-induced elevations in MCOGs and CTHs for Ns and DCC clouds are observed, the effect of meteorology cannot be completely ruled out, which merits further analysis.

1. Introduction

Aerosols can play an important role in Earth's climate by altering the energy and water cycles (Ramanathan et al. 2001; Rosenfeld et al. 2014). Various effects have been proposed that are now broadly referred to as the aerosol–radiation interactions (ARI) and aerosol–cloud–interactions (ACI) (IPCC 2013). The mechanisms for ARI have been much better understood than ACI, even though very large uncertainties still exist in the former chiefly owing to a poor knowledge of the aerosol properties. As such, ACI has been investigated more intensively in recent years with more groundbreaking findings

Corresponding author address: Jianping Guo, State Key Laboratory of Severe Weather, Chinese Academy of Meteorological Sciences, 46 Zhong-Guan-Cun South Avenue, Haidian District, Beijing 100081, China.
E-mail: jpguo@camscma.cn

as reviewed comprehensively by Tao et al. (2012) on the ACI for convective clouds and on the aerosol invigoration effect (Altaratz et al. 2014).

It is worth noting that many of the effects originate from a fundamental effect that is generally referred to as the Twomey effect (Twomey 1977). As aerosols serve as cloud condensation nuclei (CCN), more aerosols lead to more, but smaller, cloud droplets in liquid clouds, making the clouds more reflective under constant liquid water content. As a consequence, the formation of precipitation is delayed, and cloud lifetime is prolonged accordingly (Albrecht 1989). For warm clouds, this makes it hard to trigger collision–coalescence processes, leading to a delay in droplet growth and suppression of rain formation processes (Rosenfeld 1999). For mixed-phase clouds, the inhibition of warm rain processes permits more cloud droplets to freeze and release latent heat above the 0°C isotherm and thus invigorates the growth of convective clouds (Andreae et al. 2004;

Kaufman et al. 2005; Rosenfeld et al. 2008). This enhances the growth of large hail and cold rain processes (Tao et al. 2012). Also, the vertical structure of clouds may be modified both vertically (Li et al. 2011) and horizontally (Fan et al. 2013), which in turn likely leads to variations in the dynamics and thermodynamics of cloud systems (Heiblum et al. 2012).

The Twomey effect, however, cannot be always observed (Yuan et al. 2008; Quaas et al. 2009; Grandey and Stier 2010; Wang et al. 2014). Both theoretical (e.g., Feingold et al. 2001) and observational (e.g., F. Wang et al. 2015) studies have indicated that a boomerang shape exists in the cloud response to aerosols; that is, cloud effective radius decreases and then increases as the aerosol loading increases. This is most likely due to the buffering mechanism behind the nonmonotonic response of clouds and radiation to changes in aerosols (Stevens and Feingold 2009).

ACI has been studied for different cloud regimes such as midlatitude stratus clouds over land from in situ aircraft observations (Feingold et al. 2003), Arctic stratus clouds from ground remote sensing observations (Garrett et al. 2004; Garrett and Zhao 2006), stratocumulus clouds over the eastern Pacific Ocean from airborne field campaigns (Ackerman et al. 2004; Twohy et al. 2005), warm cumulus clouds over the Gulf and the southern United States (Yuan et al. 2008), deep convective clouds (DCC) over the Atlantic Ocean (Koren et al. 2005) using satellite data and the global tropics (Niu and Li 2012; Peng et al. 2016) using A-Train satellite data, and for all types of clouds using 10 years of long-term ground observations made at the Southern Great Plains site (Li et al. 2011), among others. For all such studies, one of the most challenging tasks is to untangle the effects of meteorology and aerosols on cloud systems. Various cloud regimes are typically governed by different cloud dynamical processes, resulting in different microphysical properties (Hartmann et al. 1992; Norris 1998). Therefore, aerosol effects on the formation and development of different types of cloud differ considerably (Gryspeerdt and Stier 2012; Gryspeerdt et al. 2014).

Most of these studies are limited to ACI either at the cloud top (e.g., Klüser et al. 2008; Wang et al. 2014) or at the cloud base (e.g., Feingold et al. 2003; Painemal and Zuidema 2013). This is because these studies are chiefly based on data from either spaceborne or ground-based remote sensing instruments that cannot penetrate cloud layers. Only a few studies (e.g., Storer et al. 2014) focused on changes inside clouds induced by aerosols. Recent general circulation model simulations indicated that cloud fraction is much less sensitive to changes in aerosols compared with cloud liquid/ice content (Y. Wang

et al. 2015). This further highlights the importance of investigating the response of cloud vertical structure to aerosols. The Cloud Profiling Radar (CPR) on board *CloudSat*, flying as part of the A-Train constellation, provides height-resolved information about clouds on a global scale. This allows for statistical analyses of vertical cloud macro- and microphysical properties (Stephens et al. 2002).

Storer et al. (2014) examined the changes in the vertical structure of convective clouds with aerosol loading using the radar echoes of *Cloudsat* over the east Atlantic Ocean. Similarly, Guo et al. (2016, manuscript submitted to *J. Geophys. Res. Atmos.*) gained an insight into the influence of aerosols on the internal structure of precipitating clouds using the precipitation radar data on board the Tropical Rainfall Measuring Mission (TRMM) satellite and coincident ground-based aerosol observations. They found that convective precipitating clouds systematically shifted toward higher altitudes with increasing aerosol loading. Large uncertainty exists in estimating the response of precipitation to aerosols, which is mostly caused by the unjustified generalization of results obtained for clouds of a certain type to all clouds (Khain 2009). Therefore, it is imperative to investigate the exclusive response of a specific cloud regime to aerosols.

The goal of this study is to investigate if and how aerosols modify cloud vertical structure. The remainder of this paper proceeds as follows. The time period and region of interest to be investigated are described in section 2. The data and methodology will be introduced in section 3. The three-dimensional cloud climatology in eastern China, as well as the response of different types of clouds to aerosols in the vertical, is examined in section 4. Finally, key findings of this study are summarized in section 5.

2. Time period and region of interest

The east Asian summer monsoon and its related seasonal rain belts show a strong spatiotemporal variability on intraseasonal, interannual, and interdecadal time scales (Ding 1992). Typically, monsoon clouds cover most parts of eastern China during the warm season. Data from May to September of 2008–2010 are thus chosen for this study to ensure sufficient number of samples.

China, especially eastern China, has undergone rapid economic development in recent decades, accompanied by a prominent increase in aerosol loading over this area (Guo et al. 2011). Figure 1 shows the spatial distribution of mean atmospheric visibility observed at 0800 Beijing time (BJT) across China during the warm months for the
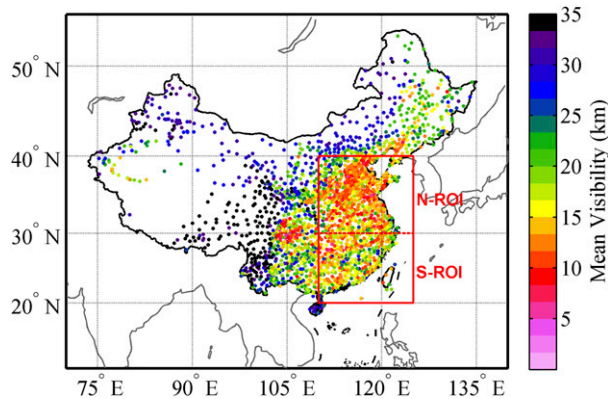
FIG. 1. The spatial distribution of mean visibility at 0800 BJT over mainland China during the warm months (from May through September) of 2008–2010. The red box outlines the ROI, divided into the N-ROI and S-ROI subdomains.

selected period. These visibility measurements are made four times a day at ground-based weather stations in China. The region of interest (ROI), namely the red box (20°–40°N, 110°–125°E), is selected for its very low visibility on average as a test bed to examine how aerosol pollution impacts clouds associated with the monsoon weather regime. Of the 2129 weather stations collecting visibility data in China, 1163 are located in the ROI. The cloud regimes differ greatly between southern and northern China because of the migration of the monsoon (Ding and Chan 2005). Therefore, the ROI is split into two subregions for further detailed analyses: a northern ROI (N-ROI) and a southern ROI (S-ROI) separated at 30°N latitude.

3. Data and methodology

a. Visibility data

Surface horizontal visibility is visually measured by human observers at the weather stations and is estimated in kilometers with respect to landmarks of known distance. Reduced visibility has been used to serve as a gross indicator for aerosol loading and CCN in ACI studies in China (Rosenfeld et al. 2007; Yang et al. 2013; Yang and Li 2014). The major advantage of visibility lies in that it can be measured under all sky conditions and at most weather stations. In comparison, aerosol optical depth (AOD), a more quantitative measure of aerosol loading in terms of light attenuation, can only be retrieved under cloud-free conditions such as those from the spaceborne passive remote sensors [e.g., the Moderate Resolution Imaging Spectroradiometer (MODIS)]. Note that for ACI studies, it is the CCN that are most relevant but its measurements are more scarce, and there exist large uncertainties in the widely adopted approach of using

AOD to approximate the CCN (Niu and Li 2012). Besides, cloud contamination and bright land surfaces can tarnish the retrieval of AOD (Li et al. 2009) as for a similar ROI used by F. Wang et al. (2015). Furthermore, active remote sensors, such as the Cloud–Aerosol Lidar with Orthogonal Polarization (CALIOP) instrument on board the *Cloud–Aerosol Lidar and Infrared Pathfinder Satellite Observation* (*CALIPSO*) platform, cannot detect aerosols underneath any thick clouds that are of particular importance to ACI studies (Li et al. 2011). The narrow scanning tracks limit the number of samples as well (Winker et al. 2007). Therefore, we use visibility measurements as a proxy for CCN in this work. For very-clean-air conditions, some observers set the visibility at 30 km while others set it to over 30 km. Using 30 km as a threshold for clean conditions may thus incur an extra uncertainty. Therefore, the highest 1% of all visibility samples (including all cases with visibilities greater than 30 km) is excluded from the analysis in this study.

Visibility measurements suffer not only from major limitations such as high uncertainty due to the nature of human observation but also from the impact of relative humidity (RH). Hygroscopic growth of aerosol particles in a high RH environment may lead to decreases in visibility measurements and underestimate the corresponding aerosol loading (Cheng and Tsai 2000; Che et al. 2007; Guo et al. 2009), so the visibility measurements have to be corrected for RH. For RH between 40% and 90%, the following correction formula proposed by Rosenfeld et al. (2007) is used:

$$\mathrm{Vis_{measured}} = \mathrm{Vis_{dry}}[0.26 + 0.4285 \log(100 - \mathrm{RH})], \quad (1)$$

where $\mathrm{Vis_{measured}}$ represents the ambient visibility as measured by observers and $\mathrm{Vis_{dry}}$ represents the visibility under dry conditions—that is, the corrected visibility. Note that visibility measurements taken when $\mathrm{RH} \geq 90\%$ are excluded from the analysis to minimize the potential impact of fog contamination (Craig and Faulkenberry 1979; Chang et al. 2009). In theory, the total value of the terms in the parentheses on the right hand should be less than one, as $\mathrm{Vis_{dry}}$ is generally greater than $\mathrm{Vis_{measured}}$. However, when RH ranges from 40% to 45%, $\mathrm{Vis_{dry}}$ is less than $\mathrm{Vis_{measured}}$. Thus, caution should be paid when correcting for visibility using Eq. (1). The number of samples belonging to this scenario (i.e., $\mathrm{Vis_{dry}} > \mathrm{Vis_{measured}}$) account for less than 2% of the total number of samples. To avoid potential noise in the following analyses, these samples have been removed.

Visibility measurements taken at 0800 and 1400 BJT are closest to the *CloudSat* overpass time of 1330 BJT.

Visibilities measured at 0800 BJT are used instead of measurements made at 1400 BJT because aerosol loading observed several hours ahead of clouds has enough time to enter and interact with clouds above, especially for convective clouds. The washout effect caused by rainfall can also be avoided in this way.

Aerosol loading varies little in a $1° \times 1°$ grid box (Anderson et al. 2003), so visibility measurements from all meteorological sites within each $1° \times 1°$ grid box defined in the ROI are averaged to represent the background aerosol conditions. Note that this mode value will reduce the occurrence frequency (OF) of extreme visibility values. Three visibility bins were defined such that each bin has an equal number of samples. The top and bottom one-third of data are defined as clean and polluted subsets, respectively. In this way, a sufficient contrast between the clean and polluted groups of data is produced while retaining good sampling statistics (Koren et al. 2012).

b. CloudSat data and its processing

The CPR is a 94-GHz near-nadir-pointing radar onboard *CloudSat* that is sensitive to the presence of liquid and ice particles. It produces two-dimensional cross sections along the satellite track (Marchand et al. 2008) with a vertical resolution of 240 m and a horizontal resolution of 1.4 km (cross track) $\times$ 1.7 km (along track). The radar reflectivity factor ranges from -30 to $20\,dBZ$ (Stephens et al. 2002). In this study, we obtain radar reflectivity data from the level-2 product called 2B-GEOPROF, which is corrected for gaseous absorption (Mace et al. 2007). The 2B-GEOPROF product also provides a cloud mask, which is used for determining the presence of cloud features and for filtering out the backscatter signal from the surface and noisy pixels. A cloudy pixel is identified when the cloud mask value is ≥ 20 (Wall et al. 2014). For deeply developed clouds, which can have a cross-sectional width reaching hundreds of kilometers (Peng et al. 2014), these profiles identified by the CPR as cloudy represent individual profiles in cloud systems rather than separate clouds. Since visibility measurements are only available over land, only cloud profiles over the continent are considered unless noted otherwise.

Aerosol-induced changes in cloud microphysics and dynamics manifest themselves in different ways, depending on many meteorological factors on top of the cloud regime concerned (van den Heever et al. 2011). The cloud regimes, including cirrus (Ci), altostratus (As), altocumulus (Ac), stratus (St), stratocumulus (Sc), cumulus (Cu), nimbostratus (Ns), and DCC, are identified from the level-2 product called 2B-CLDCLASS-lidar. Note that Cu consists of both fair-weather cumulus

and cumulus congestus. Additionally, we directly obtain the top and base heights of each cloud layer in each profile from the 2B-CLDCLASS-lidar product, which uses merged CALIOP and CPR data (Wang and Sassen 2001, 2007).

Cu clouds in support of subsequent tropospheric deep convection ultimately act to moisten the boundary layer and impact both the radiative budget at the top of the atmosphere and at the surface (Augstein et al. 1973; Stevens et al. 2001). Ns clouds are one of the most important precipitating cloud types in the stratiform region of widespread continuous clouds within mesoscale convective systems and are more typically associated with frontal systems (warm fronts) in the midlatitudes (Houze 1993; Wolde and Vali 2002). Observational and modeling studies have shown that the aerosol-induced effects on DCCs have great implications for weather and climate systems (Rosenfeld et al. 2008; Koren et al. 2010a,b; Fan et al. 2013). These three types of cloud have low cloud bases and are possibly associated with relatively strong uplifting of air. Since they are more likely to interact with aerosols, these clouds are chosen for analysis. Only *CloudSat* radar reflectivity echoes simultaneously collocated with visibility measurements in $1° \times 1°$ grid boxes are used.

To see the exact three-dimensional distribution of clouds in the ROI, the horizontal OF (OF_H) and the vertical OF (OF_V) are calculated. Since multilayered clouds are hard penetrate and detect owing to signal attenuation and single-layered clouds are more easily connected with aerosols (e.g., Niu and Li 2012; F. Wang et al. 2015), only single-layered clouds will be examined in this study. As the CPR is a near-nadir-pointing radar with a narrow scanning track, there are grid boxes that are seldom overpassed by *CloudSat* when the grid size is $1° \times 1°$, inevitably leading to underestimated OF_H due to the small number of cloudy profiles detected in the grid box. To avoid this, the OF_H is calculated over $2° \times 2°$ grid boxes. Note that only the OF_H distribution is calculated over $2° \times 2°$ grid boxes, unless noted otherwise. The OF_H for a specific cloud type was calculated by dividing the occurrence number of the cloud type in a $2° \times 2°$ grid box by the total occurrence number of all cloud types in that grid box.

Continuous cloudy pixels, which are defined by cloud mask data at a vertical resolution of 240 m, constitute the segments in a profile. These segments are identified as different cloud layers, and the pixels in each layer are classified to the same cloud type. As a result, the occurrence number of each cloud type at different altitudes can be tabulated. A method similar to that proposed by Adams et al. (2012) is used to calculate the vertical OF distribution of clouds. At a given altitude in

the profile, the number of pixels in each cloud category and the total number of detected samples are first tabulated in 0.24-km bins from 0 to 25 km in each $1° \times 1°$ grid box. Then the OF_V of each cloud type is calculated by dividing the number of pixels in each cloud category by the total number of detected samples.

c. ERA-Interim data

Meteorological parameters are extracted from the European Centre for Medium-Range Weather Forecasts (ECMWF) interim reanalysis (ERA-Interim; Dee et al. 2011) so that environmental effects on cloud properties can be untangled from aerosol effects on cloud properties. Reanalysis data ($1° \times 1°$) at 1400 BJT are used to match the cloud features derived from *CloudSat*. Lower-tropospheric stability (LTS; calculated as the difference between potential temperatures at 700 and 1000 hPa) is used to characterize atmospheric stability (Klein and Hartmann 1993). Vertical velocities at 825, 600, and 400 hPa are used to characterize the strength of atmospheric dynamics for Cu clouds, Ns clouds, and DCC, respectively. Cloud radar reflectivity profiles and associated features are sorted into five equal-step subsets of data according to the above-mentioned meteorological parameters.

d. Normalized contoured frequency by altitude diagrams

The contoured frequency by altitude diagram (CFAD) first proposed by Yuter and Houze (1995) shows the OF distribution of certain radar reflectivity Z values at each altitude level. The CFAD is expressed as follows:

$$\text{CFAD}(i,j) = \frac{N_z(i,j)}{\sum_{j=1}^{n} N_z(i,j)}, \qquad (2)$$

where $N_z(i,j)$ is the frequency distribution function defined as the number of observations in the jth Z at the ith level. The index i goes from 1 to 125 (in intervals of 0.24 km) and the index j goes from 1 to 50 (in intervals of 1 dBZ).

Considering that spurious high OFs can occur at altitudes where there are not enough data points using the above CFAD, an improved version of the CFAD known as the normalized CFAD [NCFAD; see Fu et al. (2003) for more details] has been developed. The NCFAD is written as

$$\text{NCFAD}(i,j) = \frac{N_z(i,j)}{\sum_{i=1}^{h} \sum_{j=1}^{n} N_z(i,j)}. \qquad (3)$$

In this study, NCFADs of the differences in Z under clean and polluted conditions are examined in an attempt to detect aerosol signals in the changes in the vertical distribution of clouds and to gain insights into the possible mechanisms behind ACI in the vertical.

e. Modified center of gravity

Koren et al. (2009) have introduced the term "cloud's center of gravity" (COG) to define the height where the total cloud mass tends to concentrate. It is highly sensitive to cloud microphysical and dynamical processes (Heiblum et al. 2012) and can be used to depict the vertically weighted distribution of clouds. A greater COG means that the cloud/rain mass is concentrated at higher altitudes, suggesting that stronger convection is occurring. The COG is generally expressed as

$$\text{COG} = \frac{\sum_i H_i Z_i}{\sum_i Z_i}, \qquad (4)$$

where H_i and Z_i represent the height and radar reflectivity factor (in dBZ) at the ith level, respectively. However, negative COG values can occur under some circumstances owing to the presence of negative Z values (down to -30 dBZ) (Stephens et al. 2002). In this case, we convert Z in dBZ into Z_0 in mm^6 m^{-3} using

$$Z_0 = 10^{Z/10}. \qquad (5)$$

Based on the definition of Z regarding spherical particles (assuming Rayleigh scattering), we know that

$$Z_0 \propto D^6, \qquad (6)$$

where D is the drop diameter.

Since what we are calculating here is the COG, which is defined as the height-weighted average of droplet mass, a quantity proportional to the third power of droplet diameter will be a better proxy for droplet mass than Z_0. Therefore, the square root of Z_0 is

$$Z_1 = \sqrt{Z_0} \propto D^3. \qquad (7)$$

In this case, Z_1 is always positive. Since the gravity of clouds should be proportional to the particle volume and density, we introduce a modified center of gravity (MCOG), which is defined as

$$\text{MCOG} = \frac{\sum_i H_i Z_{1i}}{\sum_i Z_{1i}}. \qquad (8)$$

This MCOG is used in the following section to investigate the potential changes in cloud vertical distribution that are caused by aerosols.
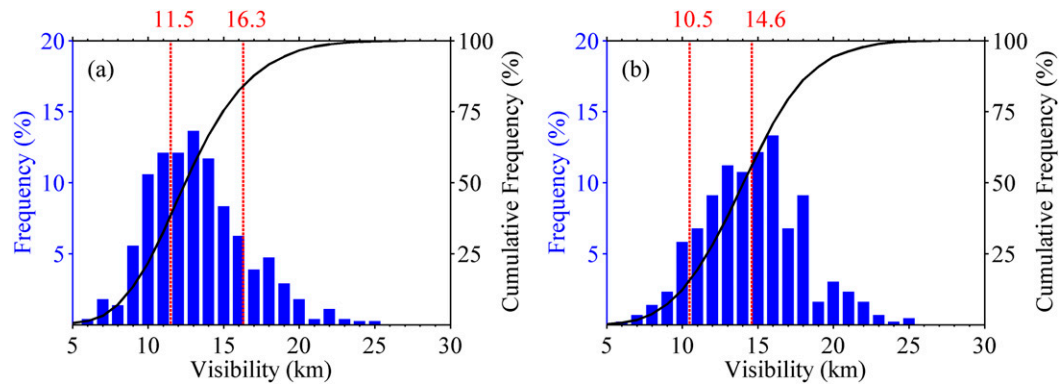
FIG. 2. Histograms of mean visibility over (a) the N-ROI and (b) the S-ROI. Blue bars represent the normalized OF in each visibility bin (1 km) and black lines represent the cumulative frequency. Red dashed lines mark the mean threshold values for clean and polluted conditions in the two subregions.

4. Results and discussion

a. Aerosols in the ROI

Figure 2 shows the normalized OF distributions of RH-corrected mean atmospheric horizontal visibility for selected cases from 2008 to 2010 in the N-ROI and S-ROI, respectively. Red dashed lines mark the mean threshold values used to define clean (15.5 and 16.7 km for the N-ROI and S-ROI, respectively) and polluted (11.3 and 12 km for the N-ROI and S-ROI, respectively) conditions. The N-ROI tends to have lower RH-corrected atmospheric visibilities (with a mean value of 13.3 km) than the S-ROI (with a mean value of 14.7 km), suggesting that aerosol pollution in the N-ROI is more serious than in the S-ROI. This agrees with results shown in Fig. 1.

b. Three-dimensional cloud climatology in eastern China

As stated in section 3b, considering both the complexity of multilayered clouds and the availability of visibility data over land, only single-layered continental clouds are considered here. In the ROI, there are 213 002 cloudy profiles over land in the warm seasons of 2008–2010, 54.4% of which are single layered. Table 1 presents statistics describing eight different types of single-layered continental clouds based on the 2B-CLDCLASS-lidar product. Profile numbers and the OFs of each type of cloud in the ROI are shown in the table. The OFs of profiles in both the N-ROI and the S-ROI are also calculated. The OFs of Cu clouds, Ns clouds, and DCC are 11.37%, 5.62%, and 6.95% in the ROI, respectively. Both Cu clouds and DCC have a relatively even distribution over the two subregions, whereas Ns clouds are more frequently found in the N-ROI.

OF_H distributions for the three types of single-layered clouds of interest in this study (Cu clouds, Ns clouds, and DCC) are shown in Fig. 3. All three cloud types have noticeable spatial variations. Cu has the largest OF_H over eastern China, reaching 8% in most parts of the ROI, particularly over the S-ROI (Fig. 3a). This may be associated with the trade wind circulation that supports the formation of shallow and low-level Cu clouds in lower-latitude zones (Stevens et al. 2001; Xue et al. 2008). The geographical distributions of Ns clouds and DCC (precipitating clouds) are shown in Figs. 3b and 3c, respectively. Ns clouds are more frequently found in the

TABLE 1. The number of cloud profiles and OFs of eight types of single-layered cloud identified over land areas in eastern China and the two subregions (N-ROI and S-ROI) during the period from 2008 to 2010. The rows that are in bold font highlight the three major cloud types investigated in the study.

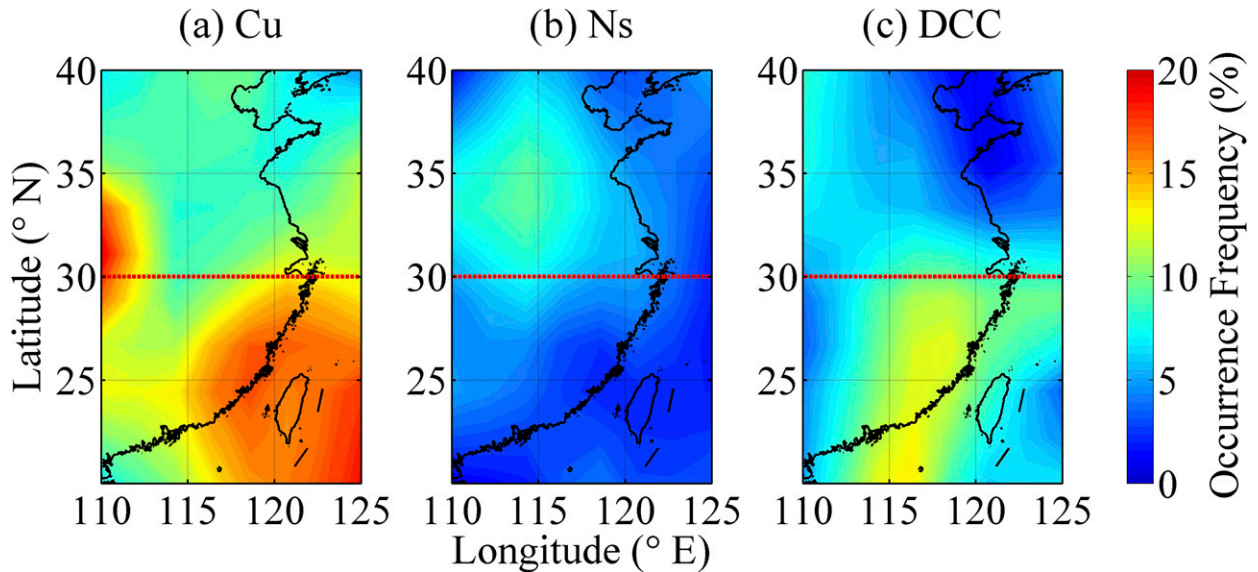|	Total		N-ROI		S-ROI	
Cloud type	No. of profiles over land	OF (%)	No. of profiles over land	OF (%)	No. of profiles over land	OF (%)
Ci	32 080	27.72	20 616	64.26	11 464	35.74
Sc	22 768	19.68	12 557	55.15	10 211	44.85
Ac	19 115	16.52	11 197	58.58	7918	41.42
Cu	**13 161**	**11.37**	**6318**	**48.01**	**6843**	**51.99**
As	13 123	11.34	10 162	77.44	2961	22.56
DCC	**8048**	**6.95**	**3076**	**38.22**	**4972**	**61.78**
Ns	**6505**	**5.62**	**4612**	**70.9**	**1893**	**29.1**
St	917	0.79	514	56.05	403	43.95

FIG. 3. Distributions of OF_H for single-layered (a) Cu clouds, (b) Ns clouds, and (c) DCC in the ROI. Red dashed lines mark the edge of the N-ROI and the S-ROI. Data (during May–September of 2008–10) are from the 2B-CLDCLASS-lidar product. The horizontal resolution is $2° \times 2°$.

N-ROI. Since extratropical cyclones primarily associated with summer-season storm-track systems in the Northern Hemisphere do not have much effect in this region during the summer monsoon (Mesquita et al. 2008), these clouds are referred to as stratiform regions in mesoscale convective systems. DCC, on the other hand, are predominantly found in the S-ROI, which is within the intertropical convergence zone (ITCZ) and its adjacent subtropical latitudes.

Figure 4 shows the zonal- and meridional-mean OF_V for the three cloud types of interest. Overall, the cloud base heights of these three types of cloud are relatively low. Compared with Ns clouds and DCC, the development of Cu clouds tends to be more constrained with lower cloud tops (mostly below 6 km), likely resulting from shallow Cu clouds, which constitute a relatively large proportion of all Cu cloud profiles. Over the ROI, Cu clouds tend to occur between 24° and 33°N (Fig. 4a) and with a large fraction (over 10%) extending vertically to about 6 km. However, Cu clouds north of 36°N have a relatively lower cloud top with over 10% of them occurring below 3 km. Along the west–east direction (Fig. 4b), the region centered at 115°E is surrounded by high OFs of cloud to the east (likely owing to the abundant vapor supply from the neighboring ocean that facilitates the formation of shallow Cu clouds) and to the west (likely owing to the combined effects of the Indian monsoon and the Tibetan Plateau). Figure 4c shows that there are more frequently occurring Ns clouds north of 30°N that can reach up to 15 km in altitude (Fig. 4d).

OF_V is concentrated below 10 km in altitude and over the land area. DCC have cloud tops as high as 18 km. Over 50% of clouds with cloud tops higher than 15 km are identified as DCC. Associated with the ITCZ present in warm months (Fig. 4e), there are more DCC in the S-ROI at lower altitudes. Also, the specific prevalence of cloudiness during the boreal warm season over the ROI is probably closely associated with the seasonal development and propagation of the mei-yu front (Lau et al. 1988; Ding 1992).

Monthly variations in zonal mean OF_H for Cu clouds, Ns clouds, and DCC are shown in Fig. 5. Both Cu clouds and DCC tend to develop gradually northward in terms of OF_H (Figs. 5a and 5c). The migration of the large OF_H belt is more obvious for DCC, from about 20°–25°N in May to 27°–32°N in August, which agrees well with typical features of the east Asian monsoon. Large OF_H values for Ns clouds are also found north of 30°N, characterized by a migration of cloudy belt from 32°–37°N in May to 35°–40°N in August. This march of the monsoon usually leads to a rain belt propagating from southern China to the Yangtze River basin in June and finally to northern China in July and August. In September, the maximum in the OF_H for DCC weakens and moves back to the south because the rain belt moves southward (between 26° and 29°N) when the monsoon period ends. Additionally, large OF_H for Ns clouds are found between 20° and 36°N in May and June, which is likely due to the persistent mei-yu front, characterized by the presence of Ns clouds, located in this region.
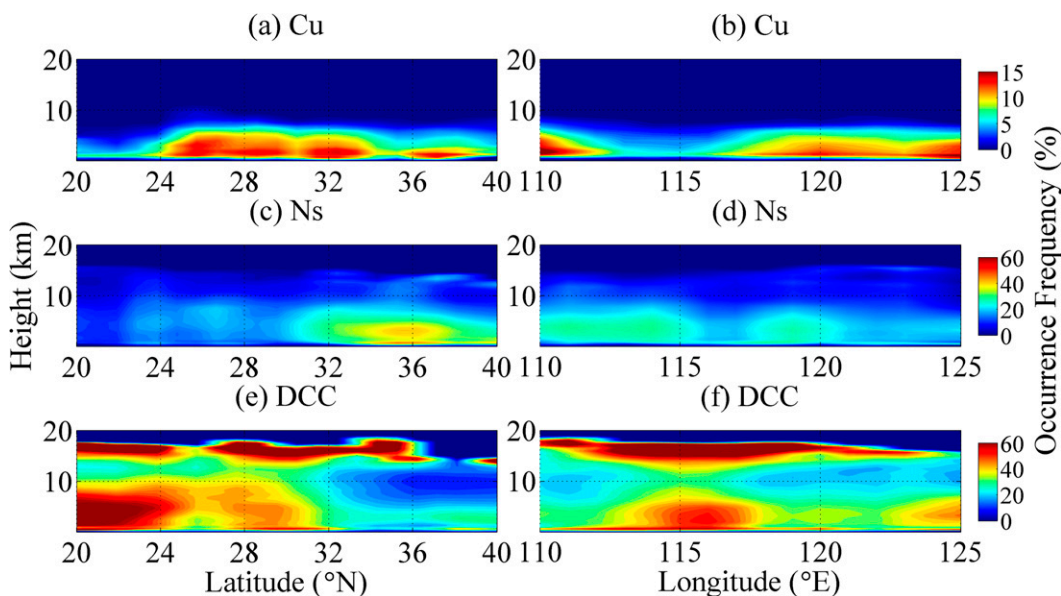
FIG. 4. Distributions of (left) zonal and (right) meridional mean OF_V for (a),(b) Cu clouds, (c),(d) Ns clouds, and (e),(f) DCC in the ROI. Note that there is a change in the scale of color bar with respect to Cu cloud vs Ns cloud and DCC.

c. Changes in cloud vertical structure associated with aerosols

The NCFADs of the cloud OF differences between clean and polluted conditions are shown in Fig. 6, which are plotted by contouring the OF difference in Z (in 1-dBZ bins) as a function of altitude (in 0.24-km bins). The Z values in the ranges from -25 to -20, -15 to -10, and 0 to 10 dBZ correspond to cloud, drizzle, and rain, respectively (Suzuki et al. 2010). For the sake of better visualization, only the NCFAD of the segments between the surface and 10, 15, and 18 km are plotted for Cu clouds, Ns clouds, and DCC, respectively. Meanwhile, only those data points that exceed the 95% significance level according to the Pearson's chi-square test are considered as valid in this figure. The number of profiles with corresponding visibility measurements and the relative proportions of Cu clouds, Ns clouds, and DCC under clean and polluted conditions are summarized in Table 2.

The differential NCFAD for Cu clouds over the N-ROI (Fig. 6a) has a bimodal pattern. One cluster is centered in the lower-left corner corresponding to $Z < -20$ dBZ and echo tops below 3 km (shallow Cu). Another cluster is located in the domain corresponding to $Z > -5$ dBZ and echo tops above 5 km (deep Cu). Wang and Sassen (2007) have argued that Cu clouds include both fair weather cumulus clouds and cumulus congestus clouds. Because shallow and deep Cu clouds show different responses to increases in aerosol loading (Fig. 6a), their responses to aerosols are analyzed separately.

There is a significant decrease ($\sim$0.2%) in OFs within the shallow Cu zone in contrast to the increase seen in the deep Cu zone as the atmosphere changes from clean to polluted (Fig. 6). This suggests that a clean
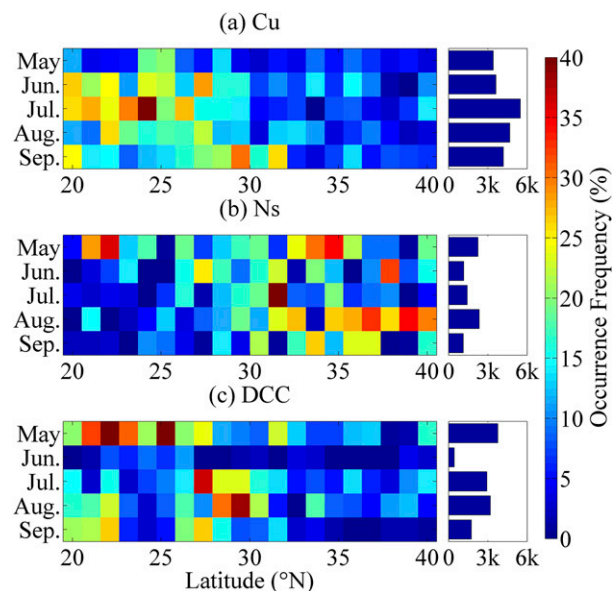

FIG. 5. Latitude–month cross sections of zonal-mean cloud fraction (%), calculated over the longitude belt of 110°–125°E, for (a) single-layered Cu clouds, (b) Ns clouds, and (c) DCC. Data are from May through September of 2008–10. Note that *CloudSat* data (especially for DCC) are not available during the period 2–8 Jun 2010. The number of samples in each month (in thousands) is given in the horizontal bar plot on the right side of each subpanel.
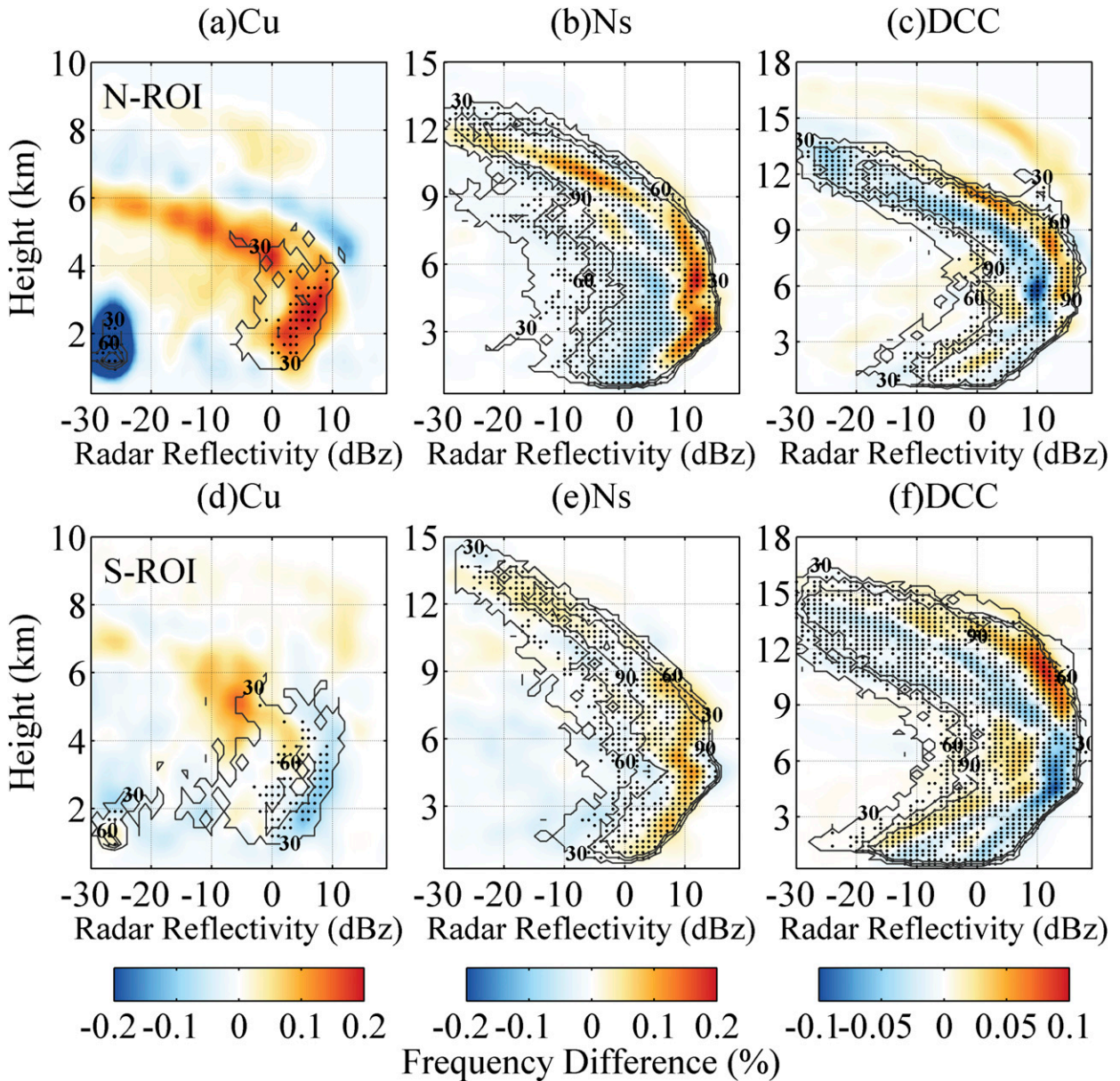
FIG. 6. Normalized contoured frequency by altitude diagrams of the difference (polluted minus clean subsets of data) in the occurrence frequency of cloud echoes from (a),(d) Cu clouds, (b),(e) Ns clouds, and (c),(f) DCC. Data are from May through September of 2008–10. Data from the (top) N-ROI and (bottom) S-ROI are shown. The black dots mark the grid points where the difference exceeds the 95% significance level ($p < 0.05$) according to the Pearson's chi-square test. The black lines with numbers show the two-dimensional contour of the number of observations.

environment tends to facilitate the formation of shallow Cu, while polluted conditions favor the development of deep Cu. This phenomenon is in good agreement with model simulation results, showing that a higher aerosol loading leads to more enhanced deep Cu and more suppressed shallow Cu clouds (Lee et al. 2008; van den Heever et al. 2011; Saleeby et al. 2015). Clouds in the S-ROI show a weaker difference between clean and polluted conditions (Fig. 6d) than do clouds in the N-ROI. However, a clear feature is seen: OF differences are positive around 4 km (the freezing level) below 5 dBZ and negative in the range of 0–10 dBZ below 4 km. One explanation could be that aerosols tend to transport more droplets to well above the freezing level, and thus more freezing of droplets will invigorate convection (Koren et al. 2014).

TABLE 2. The number of cloud profiles with visibility measurements and their corresponding percentages P to the total number of single-layered Cu clouds, Ns clouds, and DCC profiles over the N-ROI and the S-ROI. For each cloud, the number of cloud profiles and their proportion (CP) under clean and polluted conditions are also shown.

Region	Cloud type	Total		Clean		Polluted	
		No. of profiles	P (%)	No. of profiles	CP (%)	No. of profiles	CP (%)
N-ROI	Cu	1390	22.00	644	46.33	325	23.38
	Ns	1312	28.45	426	32.47	331	25.23
	DCC	1440	46.81	366	25.42	361	25.07
S-ROI	Cu	1599	23.37	536	33.52	548	34.27
	Ns	1140	60.22	414	36.32	233	20.44
	DCC	2858	57.48	1064	37.23	1035	36.21

OF changes in Ns clouds from clean to polluted environments in both subregions are shown in Figs. 6b and 6e. Differences between clean and polluted profiles show a distinct shift in OFs in zones with Z between -10 and $10\,dBZ$ and altitudes extending from 1.5 to 9 km, changing from weak negative values to pronounced positive values. Because Ns clouds are believed to constitute the stratiform region of a deeply developed mesoscale system and to contribute to about half of the precipitation produced by deep convective systems (Wolde and Vali 2002), the intensification of rain in deep convective systems could be due to aerosols. This is consistent with results presented by Storer et al. (2014), who showed that stratiform regions are more active in the presence of more aerosols.

Except for its more pronounced bow shape, NCFADs for DCC are similar to the shape of NCFADs for Ns clouds. The bulging part associated with $Z > 15\,dBZ$ could represent signals from large precipitation-sized particles present before attenuation occurs, while the tail near the surface associated with very small reflectivity values is likely due to the severe attenuation of radar signals by heavy rains above. A noticeable increase in cloud height and the presence of large Z at higher levels is seen in both subregions (Figs. 6c and 6f) when conditions go from clean to polluted. This suggests that polluted DCC are more capable of transporting larger particles and/or a greater number of hydrometeors to higher altitudes. At this point, we speculate that more latent heat is released which may further fuel convective updrafts (Williams et al. 2002; van den Heever et al. 2006; Fan et al. 2007). This updraft due to latent heat release is highly dependent on the altitudes where the aerosol microphysical effect comes into play. Recent cloud-resolving model studies have shown the magnitude of latent heat release by cold-/mixed-phase processes is up to about an order of magnitude smaller than those in the warm-phase processes as the presence of aerosols affect collision–coalescence/condensation processes (Storer and Van den Heever 2013).

The inhomogeneous phenomena above the freezing level in Fig. 6 could be due to the differences in riming efficiency as a function of aerosols. Typically, shifting droplet sizes toward smaller diameters under higher aerosol loading increases the number of droplets available to be captured or collected. But in some extreme cases, the mean diameter of cloud droplets can become so small that cloud droplets are swept around the edges of the rimer and therefore the growth rate of graupel decreases (e.g., Johnson and Houze 1987; Rogers and Yau 1989; Pruppacher and Klett 1996).

In contrast, a more rapid decrease in Z at lower altitudes is found under polluted conditions. This is possibly indicative of an increase in attenuation of the radar signals, likely caused by heavier precipitation at lower levels (Luo et al. 2014). Note that Fig. 6c (and less so in Fig. 6f) shows positive maxima in OF difference near 0 below 6-km altitude, which supports the speculation about attenuation. Also, the Mie scattering due to the hydrometeors likely contributes to the lack of returns near and below the freezing level for DCC profiles, which warrants a further analysis.

To characterize internal Z differences in cloud radar echoes under polluted versus clean conditions in a more straightforward way, the MCOG and cloud-top height (CTH) are examined at great length. A nonparametric method called Spearman's rank correlation coefficients (Wilks 2011) is used to assess the correlation between visibility and MCOG and CTH. As summarized in Table 3,

TABLE 3. Spearman's rank correlation coefficients based on the dependence between the MCOG (CTH) and ground-based observed visibility for each cloud type. Note that numbers that are statistically significant at the 95% level are in boldface.

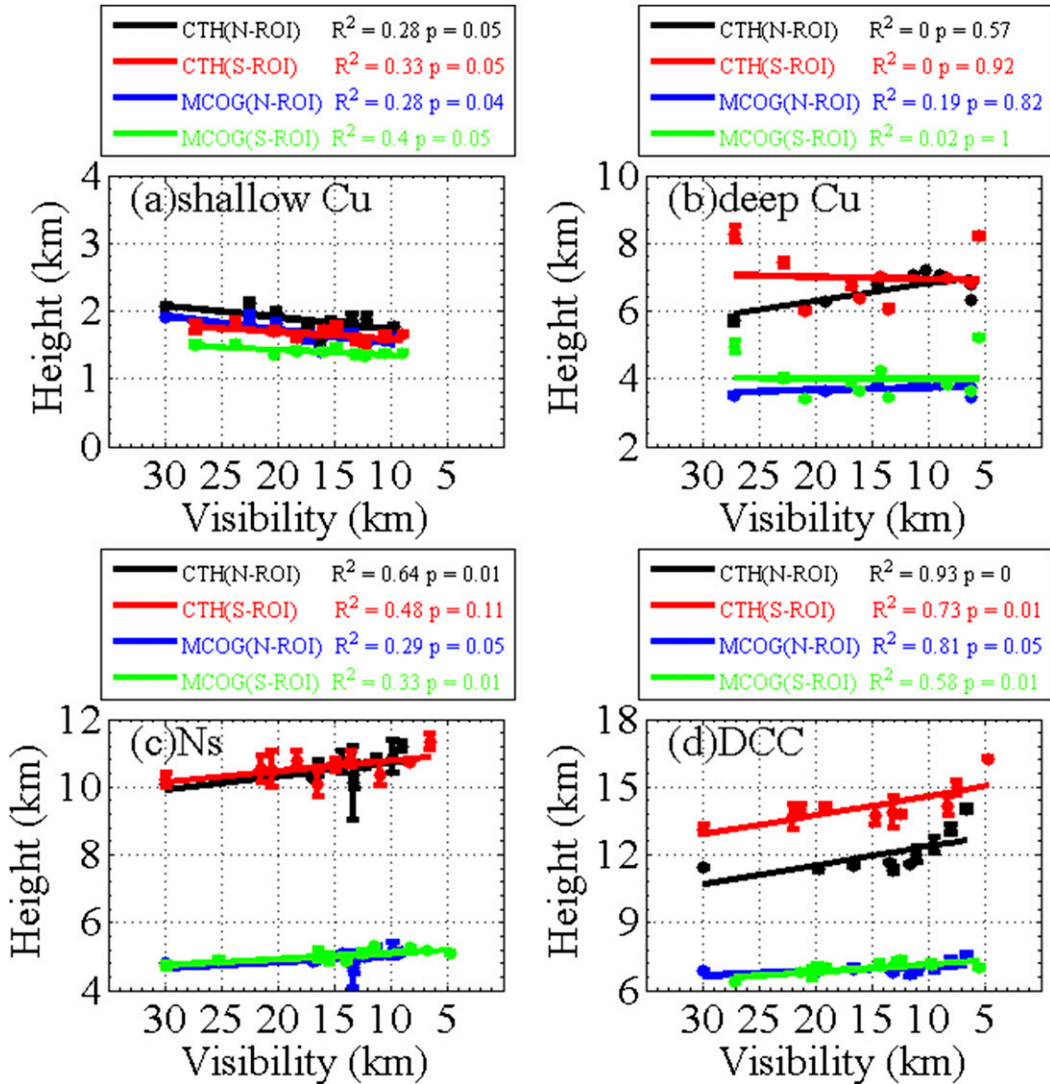|	Region	Shallow Cu	Deep Cu	Ns	DCC
MCOG	N-ROI	**−0.6848**	0.0924	**0.6242**	**0.6000**
	S-ROI	**−0.6121**	0.006	**0.7939**	**0.7697**
CTH	N-ROI	**−0.5636**	0.2185	**0.8303**	**0.8424**
	S-ROI	**−0.5758**	−0.0424	0.3929	**0.8061**

FIG. 7. Mean MCOG (solid lines) and CTH (dashed lines) in both ROIs as a function of mean visibility for (a) shallow Cu clouds, (b) deep Cu clouds, (c) Ns clouds, and (d) DCC. Black and red lines correspond to the regression lines from the N-ROI and the S-ROI datasets, respectively. Ten equal-population visibility bins are defined in each panel. There are roughly 150, 90, 100, and 150 samples in each bin for (a)–(d), respectively. The standard error ($\sigma/\sqrt{n}$, where n is the number of samples in each visibility bin and σ is the standard deviation of MCOG in each bin) is shown as error bars.

both MCOG and CTH within shallow Cu clouds are negatively associated with visibility in both subregions, as opposed to the overall positive correlation within Ns clouds and DCC. Since the correlations are statistically significant, the trends cannot simply be attributed to noise. By comparison, trends within deep Cu clouds are not clearly seen because of the insignificant correlation.

Figure 7 visualizes how the MCOG and CTH vary with visibility in the N-ROI and S-ROI for the three cloud types of interest. The decreasing linear regression lines are distinct for shallow Cu clouds, indicative of a likely suppression effect by aerosols. This is in general

agreement with the NCFAD shown in Fig. 6 and modeling results concerning suppressed shallow clouds (Feingold et al. 2005; Xue et al. 2008). On the contrary, significantly upward trends are pronounced for Ns clouds and DCC as aerosol loading increases. This suggests that more hydrometeors in polluted clouds are transported to higher altitudes. Given that both Ns clouds and DCC are from deeply developed convective systems, the aerosol invigoration effect for deep convection may explain this feature (Wang 2005; Teller and Levin 2006). These results may also constitute evidence supporting the idea that aerosols aid the transition from
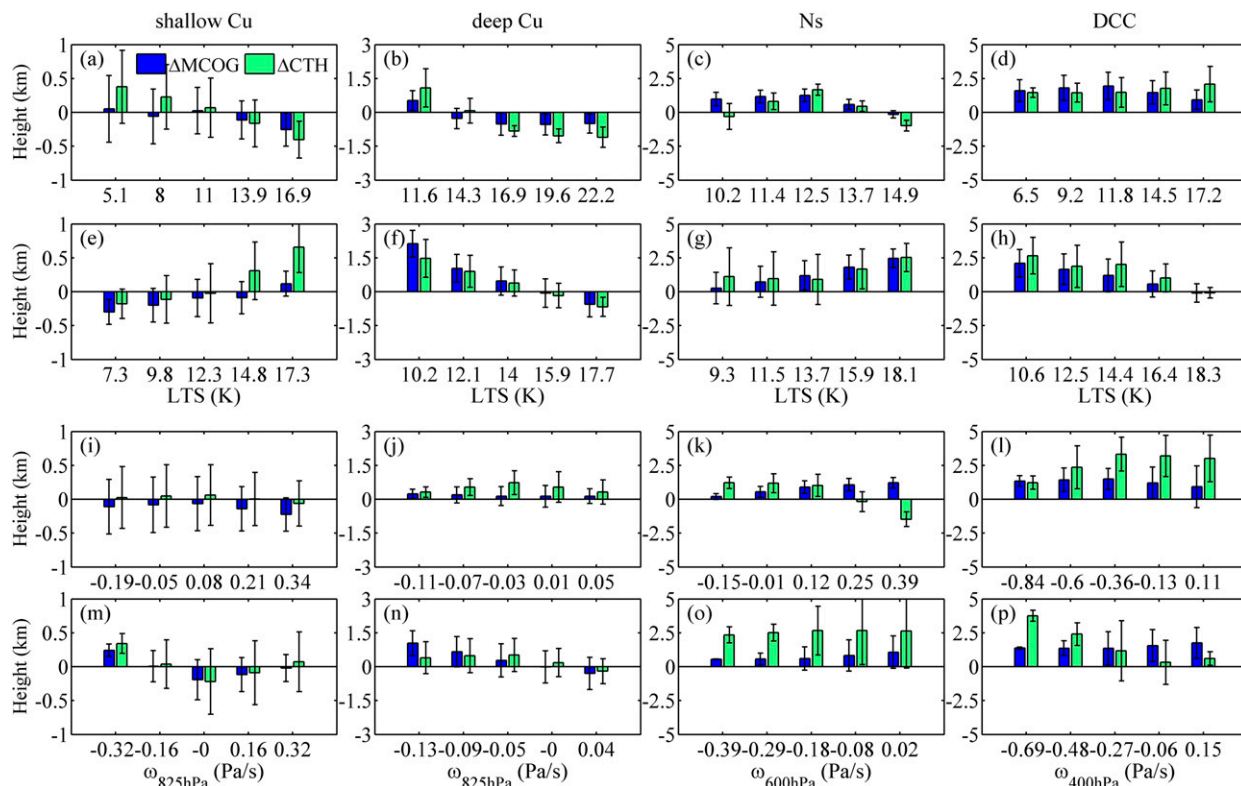
FIG. 8. MCOG and CTH differences (ΔMCOG and ΔCTH) as a function of LTS for (a),(e) shallow Cu clouds, (b),(f) deep Cu clouds, (c),(g) Ns clouds, and (d),(h) DCC for (a)–(d) the N-ROI and (e)–(h) the S-ROI. ΔMCOG and ΔCTH as a function of ω at 825 hPa for (i),(m) shallow Cu clouds and (j),(n) deep Cu clouds, (k),(o) at 600 hPa for Ns clouds, and (l),(p) at 400 hPa for DCC for (i)–(l) the N-ROI and (m)–(p) the S-ROI. Data are from May through September of 2008–10. Negative ω refers to upward motion. The difference is denoted by polluted minus clean subsets of data. Vertical error bars represent one standard deviation.

shallow to deep convective modes in terms of convective evolution (e.g., van den Heever et al. 2006; Rosenfeld et al. 2008; Li et al. 2013; Sheffield et al. 2015). To some extent, the phenomenon observed here could be one of the factors explaining the intensified heavy rainfall and lightning events observed in eastern China in recent years, which are largely formed in deep convection (Guo et al. 2014, 2016).

d. Environmental dependence

The MCOGs and CTHs are separated by LTS and vertical velocity ω in an attempt to isolate the signal attributed to aerosol loading from that attributed to environmental forcing. The LTS is calculated as the difference between potential temperatures at 700 and 1000 hPa. The ω at the following pressure levels were chosen for investigation of the dependence of aerosol–cloud interaction on atmospheric environment: 825 hPa for shallow and deep Cu clouds, 600 hPa for Ns clouds, and 400 hPa for DCC. The roles of these environmental factors in the development of MCOG and CTH

under clean and polluted conditions are examined in Figs. 8–10.

Figure 8 shows MCOG and CTH differences (ΔMCOG and ΔCTH, respectively) between the clean- and polluted-cloud profiles (polluted minus clean) of shallow and deep Cu clouds, Ns clouds, and DCCs as a function of LTS (top two rows) and ω (bottom two rows) under polluted and clean conditions. However, the differences of MCOGs and CTHs between polluted and clean clouds cannot distinctly reveal the overall sensitivity of clouds to aerosols in stratified meteorological environments. As such, Figs. 9 and 10 are presented to show how MCOGs and CTHs change as a function of visibility for different ranges of LTS and ω over N-ROI and S-ROI, respectively. In Fig. 9, samples were sorted according to LTS and ω in each 1° × 1° grid box, then divided into three bins (low, medium, and high), each containing the same number of samples. As shown in these figures, for different types of clouds, the responses of MCOGs and CTHs differ greatly to both aerosol loading and environmental conditions, which will be
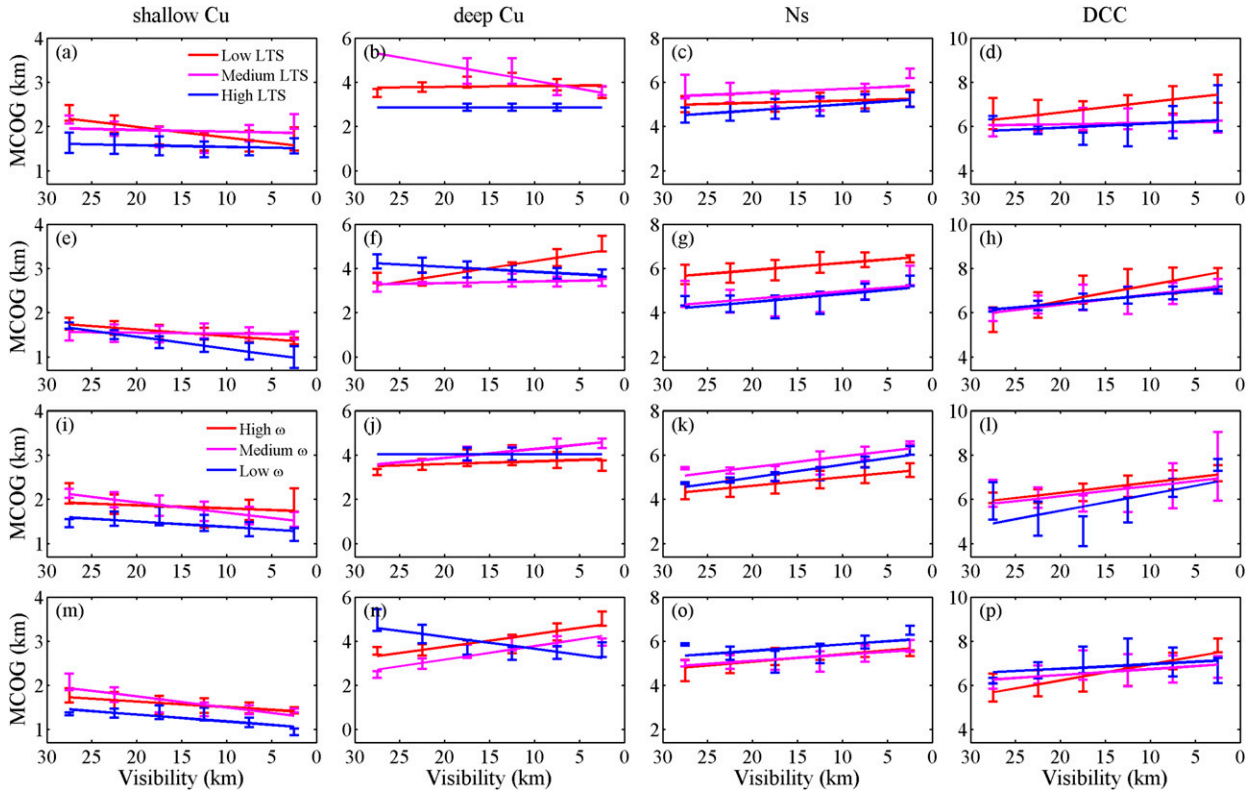
FIG. 9. MCOG for (a),(e),(i),(m) shallow Cu clouds, (b),(f),(j),(n) deep Cu clouds, (c),(g),(k),(o) Ns clouds, and (d),(h),(l),(p) DCC as a function of visibility for three equal-population bins of LTS and vertical velocity in (a)–(d),(i)–(l) the N-ROI and (e)–(h),(m)–(p) the S-ROI.

elucidated with regard to various cloud types in the following subsections.

1) SHALLOW CU CLOUDS

Overall, the MCOG for polluted shallow Cu clouds tends to be smaller compared with that for pristine shallow Cu clouds, which is most likely indicative of a slight suppression of shallow Cu clouds. MCOGs and CTHs decrease slightly with increasing aerosol loading, and the changes in MCOG and CTH with respect to visibility reach up to roughly 1 km, regardless of the magnitudes of LTS and ω. All these patterns observed in Figs. 8–10 point to the suppression effect of aerosol on shallow Cu clouds, and this effect is, to some extent, independent of the environment forcing.

2) DEEP CU CLOUDS

The MCOGs for deep Cu clouds do not show any persistent trends as the atmosphere changes from clean to polluted conditions over the two subregions (Fig. 8). When the atmosphere is less thermodynamically stable (with lower LTS or higher ω), the MCOG tends to be elevated and vice versa. The CTHs for polluted deep Cu clouds are slightly elevated over both ROIs, especially

when the atmosphere gets unstable. This is likely because deep Cu clouds in a less stable environment tend to develop into DCC. The stronger uplifting of air may lead to a stronger aerosol invigoration effect, similar to results as derived from ground-based ARM data (Li et al. 2011). In contrast, the overall trend in MCOG variation is much more distinct (Fig. 9); MCOGs for deep Cu clouds increase as aerosol loading increases in the medium and low LTS (or medium and high ω) regimes but decrease for the high LTS (or low ω) regime, especially in the S-ROI. This suggests that lower values of LTS are associated with a more unstable atmosphere and vertically developed clouds. Similar to MCOGs, CTHs of deep Cu clouds also show upward trends in a more stable environment (Fig. 10).

3) NS CLOUDS

As for Ns clouds, the enhancement in both CTHs and MCOGs can be seen noticeably regardless of changes in LTS and ω (Fig. 8), especially in the S-ROI, which is generally consistent with the results in Fig. 7 and Table 3. The pervasive aerosol-induced invigoration in DCC has been reported in numerous studies (e.g., Koren et al. 2010a; Li et al. 2011), and the Ns clouds can be typically
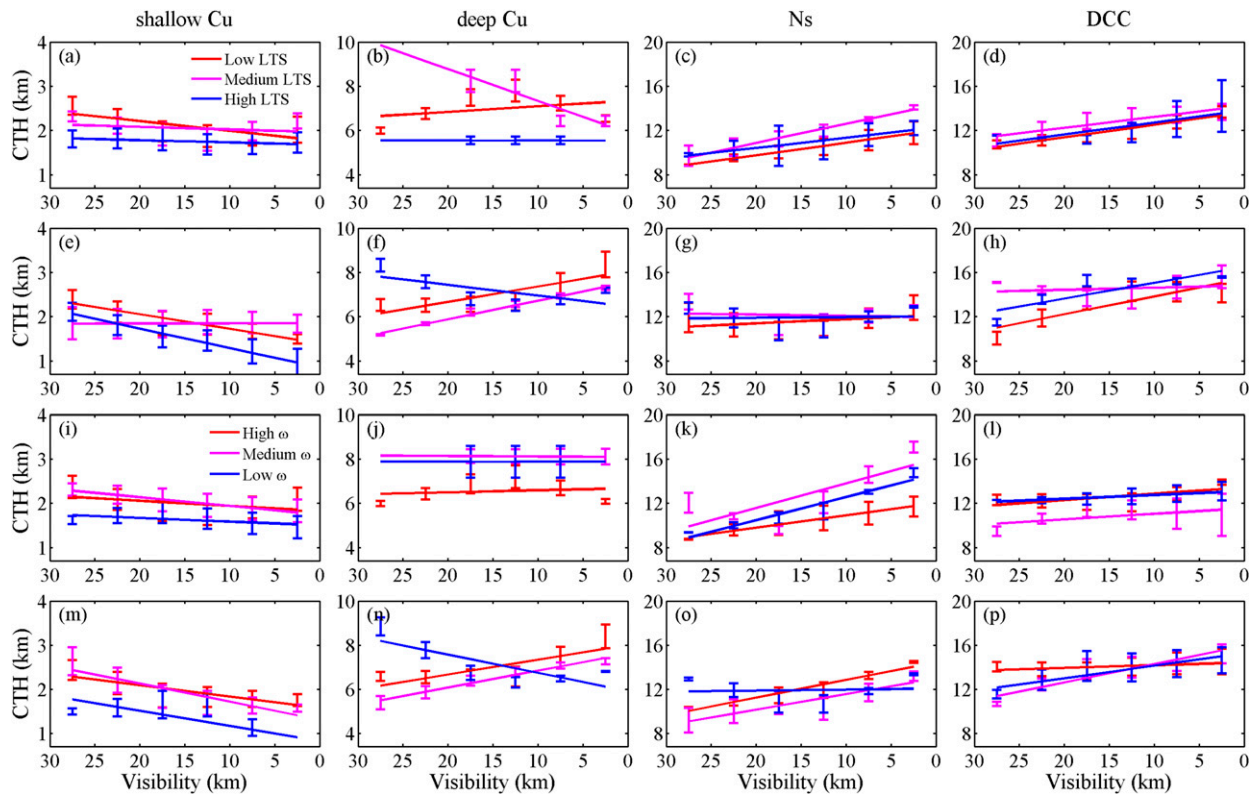
FIG. 10. As in Fig. 9, but for CTH.

found in the stratiform regions of DCC. Therefore, the strengthened development of DCC due to aerosols can partly account for the enhancement of CTH and MCOG for Ns clouds. Also, significant upward trends can also be found in Figs. 9 and 10, further suggesting that the stratiform regions of deep convective systems could have a stronger elevation in a more polluted environment regardless of environmental conditions.

4) DCC

The CTHs and MCOGs for polluted DCC seem to be consistently higher than in a pristine environment. These independent changes in different LTS and ω bins suggest that the aerosol invigoration effect favors DCC. Also, comparing to the less variation of MCOG and CTH for shallower clouds (shallow Cu and deep Cu clouds), this noticeable pattern maybe indicates that the aerosol effect is independent of the thermodynamic changes, especially for deeply developed clouds in a convective system (Ns clouds and DCC). Although the effect of convective invigoration seems evident under low LTS condition (Figs. 9 and 10), MCOG and CTH variation trends are generally less clear for DCC under medium- and high-LTS conditions, indicating both MCOG and CTH exhibit a near-orthogonal dependence

on aerosols and the environment. In other words, this suggests the atmospheric thermodynamic condition, on top of the observed aerosol effect here, plays a significant role in the cloud vertical development.

5. Conclusions

Eastern China has experienced severe air pollution (characterized by low horizontal visibility), so it provides an ideal test bed for studies of aerosol impacts on clouds. This study provides evidences of how the vertical structure of clouds responds to the aerosol impacts by viewing snapshots of clouds. Aerosol–cloud interactions in three different cloud regimes (single-layered Cu clouds, Ns clouds, and DCC) over this region have been investigated. Cloud data from standard *CloudSat* products and simultaneous ground-based horizontal visibility observations are used to determine any possible influences of aerosol perturbations to cloud vertical structure. Analyses show that the high aerosol loading in this area can lead to dramatic modifications of cloud features over this region.

Given the rain belt migration during the summer monsoon the analysis concerning the aerosol impact on the vertical structure of Cu clouds, Ns clouds, and DCC

has been done over two subregions (N-ROI and S-ROI) in eastern China. The analysis revealed strengthened rainfall for Ns clouds and invigorated development for DCC by aerosols, although the meteorology effect at this point cannot be ruled out. More vigorous deep Cu clouds and weak shallow Cu clouds are also found to be influenced by aerosols.

Correlations analyses between MCOG/CTH and visibility also indicate that the aerosol indirect effect has a relatively large impact on shallow Cu clouds, Ns clouds, and DCC. Shallow Cu clouds are inhibited while deep clouds, such as Ns clouds and DCC, show the opposite. However, no significant change in MCOG/CTH is found for deep Cu clouds. The independence of aerosol effect on thermodynamical conditions is tested by investigating the responses of MCOG and CTH to aerosols with respect to LTS and ω. Results suggest that the aerosol invigoration effect is occurring in deep convective systems irrespective of thermodynamical conditions. Further analyses of MCOG and CTH trends as visibility decreases under different environmental forcing conditions also show that changes in cloud properties due to aerosol perturbations seem to be appreciable, but there is still a large component of noise due to incomplete sampling. The slopes of the relationships between convective intensity metrics (MCOG and CTH) and aerosols remain somewhat similar for different stratifications of environmental factors, and the magnitudes of each convective intensity metric increase systematically for changes in environmental factors indicating simultaneous dependence. Therefore, the influence of meteorology on clouds cannot be totally ruled out for DCC.

Although evidence has been found to support the idea that aerosols influence the development of different types of clouds, the physical mechanisms leading to these results are still not certain. Whether the observed invigoration of clouds is the result of the warm-phased or cold-phased effect is still unclear. The physical mechanisms behind the invigoration of clouds still need to be further investigated. Furthermore, to determine aerosol-induced changes in cloud microphysical parameters in the vertical more accurately, a combination of data from collocated observing active sensors and ground-based measurements, along with aerosol and cloud measuring sensors mounted on aircraft, are needed. In addition, continuous measurements of cloud droplet size and drop size distributions will help toward understanding the microphysical effects of aerosols on the lifetime of clouds.

REFERENCES

Ackerman, A. S., M. P. Kirkpatrick, D. E. Stevens, and O. B. Toon, 2004: The impact of humidity above stratiform clouds on indirect aerosol climate forcing. *Nature*, **432**, 1014–1017, doi:10.1038/nature03174.

Adams, A. M., J. M. Prospero, and C. Zhang, 2012: *CALIPSO*-derived three-dimensional structure of aerosol over the Atlantic Basin and adjacent continents. *J. Climate*, **25**, 6862–6879, doi:10.1175/JCLI-D-11-00672.1.

Albrecht, B. A., 1989: Aerosols, cloud microphysics, and fractional cloudiness. *Science*, **245**, 1227–1230, doi:10.1126/science.245.4923.1227.

Altaratz, O., I. Koren, L. A. Remer, and E. Hirsch, 2014: Review: Cloud invigoration by aerosols—Coupling between microphysics and dynamics. *Atmos. Res.*, **140–141**, 38–60, doi:10.1016/j.atmosres.2014.01.009.

Anderson, T. L., R. J. Charlson, D. M. Winker, J. A. Ogren, and K. Holmén, 2003: Mesoscale variations of tropospheric aerosols. *J. Atmos. Sci.*, **60**, 119–136, doi:10.1175/1520-0469(2003)060<0119:MVOTA>2.0.CO;2.

Andreae, M., D. Rosenfeld, P. Artaxo, A. Costa, G. Frank, K. Longo, and M. Silva-Dias, 2004: Smoking rain clouds over the Amazon. *Science*, **303**, 1337–1342, doi:10.1126/science.1092779.

Augstein, E., H. Riehl, F. Ostapoff, and V. Wagner, 1973: Mass and energy transports in an undisturbed Atlantic trade-wind flow. *Mon. Wea. Rev.*, **101**, 101–111, doi:10.1175/1520-0493(1973)101<0101:MAETIA>2.3.CO;2.

Chang, D., Y. Song, and B. Liu, 2009: Visibility trends in six megacities in China 1973–2007. *Atmos. Res.*, **94**, 161–167, doi:10.1016/j.atmosres.2009.05.006.

Che, H., X. Zhang, Y. Li, Z. Zhou, and J. J. Qu, 2007: Horizontal visibility trends in China 1981–2005. *Geophys. Res. Lett.*, **34**, L24706, doi:10.1029/2007GL031450.

Cheng, M. T., and Y. I. Tsai, 2000: Characterization of visibility and atmospheric aerosols in urban, suburban, and remote areas. *Sci. Total Environ.*, **263**, 101–114, doi:10.1016/S0048-9697(00)00670-7.

Craig, C. D., and G. D. Faulkenberry, 1979: The application of ridit analysis to detect trends in visibility. *Atmos. Environ.*, **13**, 1617–1622, doi:10.1016/0004-6981(79)90319-6.

Dee, D. P., and Coauthors, 2011: The ERA-Interim reanalysis: Configuration and performance of the data assimilation system. *Quart. J. Roy. Meteor. Soc.*, **137**, 553–597, doi:10.1002/qj.828.

Ding, Y. H., 1992: Summer monsoon rainfalls in China. *J. Meteor. Soc. Japan*, **70**, 337–396.

——, and J. C. L. Chan, 2005: The East Asian summer monsoon: An overview. *Meteor. Atmos. Phys.*, **89**, 117–142, doi:10.1007/s00703-005-0125-z.

Fan, J., R. Zhang, G. Li, and W.-K. Tao, 2007: Effects of aerosols and relative humidity on cumulus clouds. *J. Geophys. Res.*, **112**, D14204, doi:10.1029/2006JD008136.

——, L. R. Leung, D. Rosenfeld, Q. Chen, Z. Li, J. Zhang, and H. Yan, 2013: Microphysical effects determine macrophysical response for aerosol impacts on deep convective clouds. *Proc. Natl. Acad. Sci. USA*, **110**, E4581–E4590, doi:10.1073/pnas.1316830110.

Feingold, G., L. A. Remer, J. Ramaprasad, and Y. J. Kaufman, 2001: Analysis of smoke impact on clouds in Brazilian biomass burning regions: An extension of Twomey's approach. *J. Geophys. Res.*, **106**, 22 907–22 922, doi:10.1029/2001JD000732.

——, W. L. Eberhard, D. E. Veron, and M. Previdi, 2003: First measurements of the Twomey indirect effect using ground-based remote sensors. *Geophys. Res. Lett.*, **30**, 1287, doi:10.1029/2002GL016633.

——, H. L. Jiang, and J. Y. Harrington, 2005: On smoke suppression of clouds in Amazonia. *Geophys. Res. Lett.*, **32**, L02804, doi:10.1029/2004GL021369.

Fu, Y., Y. Lin, G. Liu, and Q. Wang, 2003: Seasonal characteristics of precipitation in 1998 over East Asia as derived from TRMM PR. *Adv. Atmos. Sci.*, **20**, 511–529, doi:10.1007/BF02915495.

Garrett, T. J., and C. Zhao, 2006: Increased Arctic cloud longwave emissivity associated with pollution from mid-latitudes. *Nature*, **440**, 787–789, doi:10.1038/nature04636.

——, ——, X. Dong, G. G. Mace, and P. V. Hobbs, 2004: Effects of varying aerosol regimes on low-level Arctic stratus. *Geophys. Res. Lett.*, **31**, L17105, doi:10.1029/2004GL019928.

Grandey, B. S., and P. Stier, 2010: A critical look at spatial scale choices in satellite-based aerosol indirect effect studies. *Atmos. Chem. Phys.*, **10**, 11 459–11 470, doi:10.5194/acp-10-11459-2010.

Gryspeerdt, E., and P. Stier, 2012: Regime-based analysis of aerosol-cloud interactions. *Geophys. Res. Lett.*, **39**, L21802, doi:10.1029/2012GL053221.

——, ——, and D. G. Partridge, 2014: Satellite observations of cloud regime development: The role of aerosol processes. *Atmos. Chem. Phys.*, **14**, 1141–1158, doi:10.5194/acp-14-1141-2014.

Guo, J.-P., and Coauthors, 2009: Correlation between PM concentrations and aerosol optical depth in eastern China. *Atmos. Environ.*, **43**, 5876–5886, doi:10.1016/j.atmosenv.2009.08.026.

——, X. Y. Zhang, Y. R. Wu, Y. Zhaxi, H. Z. Che, B. La, W. Wang, and X. W. Li, 2011: Spatio-temporal variation trends of satellite-based aerosol optical depth in China during 1980–2008. *Atmos. Environ.*, **45**, 6802–6811, doi:10.1016/j.atmosenv.2011.03.068.

——, M. Deng, J. Fan, Z. Li, Q. Chen, P. Zhai, Z. Dai, and X. Li, 2014: Precipitation and air pollution at mountain and plain stations in northern China: Insights gained from observations and modeling. *J. Geophys. Res. Atmos.*, **119**, 4793–4807, doi:10.10022013JD021161.

——, and Coauthors, 2016: Delaying precipitation and lightning by air pollution over Pearl River Delta. Part I: Observational analyses. *J. Geophys. Res. Atmos.*, **121**, 6472–6488, doi:10.1002/2015JD023257.

Hartmann, D. L., M. E. Ockert-Bell, and M. L. Michelsen, 1992: The effect of cloud type on Earth's energy balance: Global analysis. *J. Climate*, **5**, 1281–1304, doi:10.1175/1520-0442(1992)005<1281:TEOCTO>2.0.CO;2.

Heiblum, R. H., I. Koren, and O. Altaratz, 2012: New evidence of cloud invigoration from TRMM measurements of rain center of gravity. *Geophys. Res. Lett.*, **39**, L08803, doi:10.1029/2012GL051158.

Houze, R. A., Jr., 1993: *Cloud Dynamics.* Academic Press, 573 pp.

IPCC, 2013: *Climate Change 2013: The Physical Science Basis.* Cambridge University Press, 1535 pp., doi:10.1017/CBO9781107415324.

Johnson, R. H., and R. A. Houze Jr., 1987: Precipitating cloud systems of the Asian monsoon. *Monsoon Meteorology*, C.-P. Chang and T. N. Krishnamurti, Eds., Oxford Press, 298–353.

Kaufman, Y. J., I. Koren, L. A. Remer, D. Rosenfeld, and Y. Rudich, 2005: The effect of smoke, dust, and pollution aerosol on shallow cloud development over the Atlantic Ocean. *Proc. Natl. Acad. Sci. USA*, **102**, 11 207–11 212, doi:10.1073/pnas.0505191102.

Khain, A. P., 2009: Notes of state-of-the-art investigations of aerosol effects on precipitation: A critical review. *Environ. Res. Lett.*, **4**, 015004, doi:10.1088/1748-9326/4/1/015004.

Klein, S. A., and D. L. Hartmann, 1993: The seasonal cycle of low stratiform clouds. *J. Climate*, **6**, 1587–1606, doi:10.1175/1520-0442(1993)006<1587:TSCOLS>2.0.CO;2.

Klüser, L., D. Rosenfeld, A. Macke, and T. Holzer-Popp, 2008: Observations of shallow convective clouds generated by solar heating of dark smoke plumes. *Atmos. Chem. Phys.*, **8**, 2833–2840, doi:10.5194/acp-8-2833-2008.

Koren, I., Y. J. Kaufman, D. Rosenfeld, L. A. Remer, and Y. Rudich, 2005: Aerosol invigoration and restructuring of Atlantic convective clouds. *Geophys. Res. Lett.*, **32**, L14828, doi:10.1029/2005GL023187.

——, O. Altaratz, G. Feingold, Z. Levin, and T. Reisin, 2009: Cloud's center of gravity—A compact approach to analyze convective cloud development. *Atmos. Chem. Phys.*, **9**, 155–161, doi:10.5194/acp-9-155-2009.

——, G. Feingold, and L. A. Remer, 2010a: The invigoration of deep convective clouds over the Atlantic: Aerosol effect, meteorology or retrieval artifact? *Atmos. Chem. Phys.*, **10**, 8855–8872, doi:10.5194/acp-10-8855-2010.

——, L. A. Remer, O. Altaratz, J. V. Martins, and A. Davidi, 2010b: Aerosol-induced changes of convective cloud anvils produce strong climate warming. *Atmos. Chem. Phys.*, **10**, 5001–5010, doi:10.5194/acp-10-5001-2010.

——, O. Altaratz, L. A. Remer, G. Feingold, J. V. Martins, and R. H. Heiblum, 2012: Aerosol-induced intensification of rain from the tropics to the mid-latitudes. *Nat. Geosci.*, **5**, 118–122, doi:10.1038/ngeo1364.

——, G. Dagan, and O. Altaratz, 2014: From aerosol-limited to invigoration of warm convective clouds. *Science*, **344**, 1143–1146, doi:10.1126/science.1252595.

Lau, K.-M., G. J. Yang, and S. H. Shen, 1988: Seasonal and intra-seasonal climatology of summer monsoon rainfall over East Asia. *Mon. Wea. Rev.*, **116**, 18–37, doi:10.1175/1520-0493(1988)116<0018:SAICOS>2.0.CO;2.

Lee, S. S., L. J. Donner, V. T. J. Phillips, and Y. Ming, 2008: The dependence of aerosol effects on clouds and precipitation on cloud-system organization, shear and stability. *J. Geophys. Res.*, **113**, D16202, doi:10.1029/2007JD009224.

Li, X. W., W. K. Tao, H. Masunaga, G. J. Gu, and X. P. Zeng, 2013: Aerosol effects on cumulus congestus population over the tropical Pacific: A cloud-resolving modeling study. *J. Meteor. Soc. Japan*, **91**, 817–833, doi:10.2151/jmsj.2013-607.

Li, Z., and Coauthors, 2009: Uncertainties in satellite remote sensing of aerosols and impact on monitoring its long-term trend: A review and perspective. *Ann. Geophys.*, **27**, 2755–2770, doi:10.5194/angeo-27-2755-2009.

——, F. Niu, J. Fan, Y. Liu, D. Rosenfeld, and Y. Ding, 2011: Long-term impacts of aerosols on the vertical development of clouds and precipitation. *Nat. Geosci.*, **4**, 888–894, doi:10.1038/ngeo1313.

Luo, Z. J., J. Jeyaratnam, S. Iwasaki, H. Takahashi, and R. Anderson, 2014: Convective vertical velocity and cloud internal vertical structure: An A-Train perspective. *Geophys. Res. Lett.*, **41**, 723–729, doi:10.1002/2013GL058922.

Mace, G. G., R. Marchand, Q. Zhang, and G. Stephens, 2007: Global hydrometeor occurrence as observed by CloudSat: Initial observations from summer 2006. *Geophys. Res. Lett.*, **34**, L09808, doi:10.1029/2006GL029017.

Marchand, R., G. G. Mace, T. Ackerman, and G. Stephens, 2008: Hydrometeor detection using *Cloudsat*—An Earth-orbiting 94-GHz cloud radar. *J. Atmos. Oceanic Technol.*, **25**, 519–533, doi:10.1175/2007JTECHA1006.1.

Mesquita, M. D. S., N. Gunnar Kvamstø, A. Sorteberg, and D. E. Atkinson, 2008: Climatological properties of summertime extra-tropical storm tracks in the Northern Hemisphere. *Tellus*, **60A**, 557–569, doi:10.1111/j.1600-0870.2008.00305.x.

Niu, F., and Z. Li, 2012: Systematic variations of cloud top temperature and precipitation rate with aerosols over the global tropics. *Atmos. Chem. Phys.*, **12**, 8491–8498, doi:10.5194/acp-12-8491-2012.

Norris, J. R., 1998: Low cloud type over the ocean from surface observations. Part II: Geographical and seasonal variations. *J. Climate*, **11**, 383–403, doi:10.1175/1520-0442(1998)011<0383:LCTOTO>2.0.CO;2.

Painemal, D., and P. Zuidema, 2013: The first aerosol indirect effect quantified through airborne remote sensing during VOCALS-REx. *Atmos. Chem. Phys.*, **13**, 917–931, doi:10.5194/acp-13-917-2013.

Peng, J., H. Zhang, and Z. Li, 2014: Temporal and spatial variations of global deep cloud systems based on CloudSat and CALIPSO satellite observations. *Adv. Atmos. Sci.*, **31**, 593–603, doi:10.1007/s00376-013-3055-6.

——, Z. Li, H. Zhang, J. Liu, and M. Cribb, 2016: Systematic changes in cloud radiative forcing with aerosol loading for deep clouds in the tropics. *J. Atmos. Sci.*, **73**, 231–249, doi:10.1175/JAS-D-15-0080.1.

Pruppacher, H. R., and J. D. Klett, 1996: *Microphysics of Clouds and Precipitation.* Atmospheric and Oceanographic Sciences Library, Vol. 18, Springer, 954 pp.

Quaas, J., and Coauthors, 2009: Aerosol indirect effects—General circulation model intercomparison and evaluation with satellite data. *Atmos. Chem. Phys.*, **9**, 8697–8717, doi:10.5194/acp-9-8697-2009.

Ramanathan, V., P. Crutzen, J. Kiehl, and D. Rosenfeld, 2001: Aerosols, climate, and the hydrological cycle. *Science*, **294**, 2119–2124, doi:10.1126/science.1064034.

Rogers, R. R., and M. K. Yau, 1989: *A Short Course in Cloud Physics.* 3rd ed. Butterworth-Heinemann, 304 pp.

Rosenfeld, D., 1999: TRMM observed first direct evidence of smoke from forest fires inhibiting rainfall. *Geophys. Res. Lett.*, **26**, 3105–3108, doi:10.1029/1999GL006066.

——, J. Dai, X. Yu, Z. Yao, X. Xu, X. Yang, and C. Du, 2007: Inverse relations between amounts of air pollution and orographic precipitation. *Science*, **315**, 1396–1398, doi:10.1126/science.1137949.

——, U. Lohmann, G. B. Raga, C. D. O'Dowd, M. Kulmala, S. Fuzzi, A. Reissell, and M. O. Andreae, 2008: Flood or drought: How do aerosols affect precipitation? *Science*, **321**, 1309–1313, doi:10.1126/science.1160606.

——, and Coauthors, 2014: Global observations of aerosol-cloud-precipitation-climate interactions. *Rev. Geophys.*, **52**, 750–808, doi:10.1002/2013RG000441.

Saleeby, S. M., S. R. Herbener, S. C. van den Heever, and T. L'Ecuyer, 2015: Impacts of cloud droplet–nucleating aero-sols on shallow tropical convection. *J. Atmos. Sci.*, **72**, 1369–1385, doi:10.1175/JAS-D-14-0153.1.

Sheffield, A. M., S. M. Saleeby, and S. C. van den Heever, 2015: Aerosol-induced mechanisms for cumulus congestus growth. *J. Geophys. Res. Atmos.*, **120**, 8941–8952, doi:10.1002/2015JD023743.

Stephens, G. L., and Coauthors, 2002: The *CloudSat* mission and the A-Train: A new dimension of space-based observations of clouds and precipitation. *Bull. Amer. Meteor. Soc.*, **83**, 1771–1790, doi:10.1175/BAMS-83-12-1771.

Stevens, B., and G. Feingold, 2009: Untangling aerosol effects on clouds and precipitation in a buffered system. *Nature*, **461**, 607–613, doi:10.1038/nature08281.

——, and Coauthors, 2001: Simulations of trade wind cumuli under a strong inversion. *J. Atmos. Sci.*, **58**, 1870–1891, doi:10.1175/1520-0469(2001)058<1870:SOTWCU>2.0.CO;2.

Storer, R. L., and S. C. Van den Heever, 2013: Microphysical processes evident in aerosol forcing of tropical deep convective clouds. *J. Atmos. Sci.*, **70**, 430–446, doi:10.1175/JAS-D-12-076.1.

——, ——, and T. S. L'Ecuyer, 2014: Observations of aerosol-induced convective invigoration in the tropical east Atlantic. *J. Geophys. Res. Atmos.*, **119**, 3963–3975, doi:10.1002/2013JD020272.

Suzuki, K., T. Y. Nakajima, and G. L. Stephens, 2010: Particle growth and drop collection efficiency of warm clouds as inferred from joint *CloudSat* and MODIS observations. *J. Atmos. Sci.*, **67**, 3019–3032, doi:10.1175/2010JAS3463.1.

Tao, W.-K., J. P. Chen, Z. Li, C. Wang, and C. Zhang, 2012: Impact of aerosols on convective clouds and precipitation. *Rev. Geophys.*, **50**, RG2001, doi:10.1029/2011RG000369.

Teller, A., and Z. Levin, 2006: The effects of aerosols on precipitation and dimensions of subtropical clouds: A sensitivity study using a numerical cloud model. *Atmos. Chem. Phys.*, **6**, 67–80, doi:10.5194/acp-6-67-2006.

Twohy, C. H., M. D. Petters, J. R. Snider, B. Stevens, W. Tahnk, M. Wetzel, L. Russell, and F. Burnet, 2005: Evaluation of the aerosol indirect effect in marine stratocumulus clouds: Droplet number, size, liquid water path, and radiative impact. *J. Geophys. Res.*, **110**, D08203, doi:10.1029/2004JD005116.

Twomey, S., 1977: Influence of pollution on shortwave albedo of clouds. *J. Atmos. Sci.*, **34**, 1149–1152, doi:10.1175/1520-0469(1977)034<1149:TIOPOT>2.0.CO;2.

van den Heever, S. C., G. G. Carrió, W. R. Cotton, P. J. DeMott, and A. J. Prenni, 2006: Impacts of nucleating aerosol on Florida storms. Part I: Mesoscale simulations. *J. Atmos. Sci.*, **63**, 1752–1775, doi:10.1175/JAS3713.1.

——, G. L. Stephens, and N. B. Wood, 2011: Aerosol indirect effects on tropical convection characteristics under conditions of radiative–convective equilibrium. *J. Atmos. Sci.*, **68**, 699–718, doi:10.1175/2010JAS3603.1.

Wall, C., E. Zipser, and C. Liu, 2014: An investigation of the aerosol indirect effect on convective intensity using satellite observations. *J. Atmos. Sci.*, **71**, 430–447, doi:10.1175/JAS-D-13-0158.1.

Wang, C., 2005: A modeling study of the response of tropical deep convection to the increase of cloud condensation nuclei concentration: 1. Dynamics and microphysics. *J. Geophys. Res.*, **110**, D21211, doi:10.1029/2004JD005720.

Wang, F., J. Guo, Y. Wu, X. Zhang, M. Deng, X. Li, J. Zhang, and J. Zhao, 2014: Satellite observed aerosol-induced variability in warm cloud properties under different meteorological conditions over eastern China. *Atmos. Environ.*, **84**, 122–132, doi:10.1016/j.atmosenv.2013.11.018.

——, and Coauthors, 2015: Multi-sensor quantification of aerosol-induced variability in warm clouds over eastern China. *Atmos. Environ.*, **113**, 1–9, doi:10.1016/j.atmosenv.2015.04.063.

Wang, Y., J. H. Jiang, and H. Su, 2015: Atmospheric responses to the redistribution of anthropogenic aerosols. *J. Geophys. Res. Atmos.*, **120**, 9625–9641, doi:10.1002/2015JD023665.

Wang, Z., and K. Sassen, 2001: Cloud type and macrophysical property retrieval using multiple remote sensors. *J. Appl. Meteor.*, **40**, 1665–1682, doi:10.1175/1520-0450(2001)040<1665:CTAMPR>2.0.CO;2.

——, and ——, 2007: Level 2 cloud scenario classification product process description and interface control document, version 5.0. Cooperative Institute for Research in the Atmosphere, Colorado State University, 50 pp. [Available online at http://www.cloudsat.cira.colostate.edu/sites/default/files/products/files/2B-CLDCLASS_PDICD.P_R04.20070724.pdf.]

Wilks, D. S., 2011: *Statistical Methods in the Atmospheric Sciences*. 3rd ed. Elsevier, 676 pp.

Williams, E., and Coauthors, 2002: Contrasting convective regimes over the Amazon: Implications for cloud electrification. *J. Geophys. Res.*, **107**, 8082, doi:10.1029/2001JD000380.

Winker, D. M., W. H. Hunt, and M. J. McGill, 2007: Initial performance assessment of CALIOP. *Geophys. Res. Lett.*, **34**, L19803, doi:10.1029/2007GL030135.

Wolde, M., and G. Vali, 2002: Cloud structure and crystal growth in nimbostratus. *Atmos. Res.*, **61**, 49–74, doi:10.1016/S0169-8095(01)00102-8.

Xue, H., G. Feingold, and B. Stevens, 2008: Aerosol effects on clouds, precipitation, and the organization of shallow cumulus convection. *J. Atmos. Sci.*, **65**, 392–406, doi:10.1175/2007JAS2428.1.

Yang, X., and Z. Li, 2014: Increases in thunderstorm activity and relationships with air pollution in southeast China. *J. Geophys. Res. Atmos.*, **119**, 1835–1844, doi:10.1002/2013JD021224.

——, M. Ferrat, and Z. Li, 2013: New evidence of orographic precipitation suppression by aerosols in central China. *Meteor. Atmos. Phys.*, **119**, 17–29, doi:10.1007/s00703-012-0221-9.

Yuan, T., Z. Li, R. Zhang, and J. Fan, 2008: Increase of cloud droplet size with aerosol optical depth: An observation and modeling study. *J. Geophys. Res.*, **113**, D04201, doi:10.1029/2007JD008632.

Yuter, S. E., and R. A. Houze Jr., 1995: Three-dimensional kinematic and microphysical evolution of Florida cumulonimbus. Part II: Frequency distributions of vertical velocity, reflectivity, and differential reflectivity. *Mon. Wea. Rev.*, **123**, 1941–1963, doi:10.1175/1520-0493(1995)123<1941:TDKAME>2.0.CO;2.